ELSEVIER

Contents lists available at ScienceDirect

Spectrochimica Acta Part B: Atomic Spectroscopy

journal homepage: www.elsevier.com/locate/sab





Characterisation of a high-resolution spectroscopic setup for experimental determination of transition probabilities of neodymium

Pratyush Ranjan Sen Sarma * Maria Teresa Belmonte, Sara Llorente, Santiago Mar

University of Valladolid, P.° de Belén, 7, 47011 Valladolid, Spain

ARTICLE INFO

Keywords: Atomic emission spectroscopy Plasma diagnostics Rare earth elements Transition probabilities Hollow-cathode discharge Diffraction grating Spectral resolution

ABSTRACT

Accurate atomic data for lanthanides, particularly neodymium (Nd), are essential for astrophysical applications, including modelling kilonova opacity and determining stellar abundances. However, reliable experimental data for these ions remain scarce due to the spectral complexity of the lanthanides. In this study, we present a comprehensive characterisation of a high-resolution spectroscopic setup optimised for measuring transition probabilities of Nd lines. The system consists of a 1.5 m Czerny-Turner spectrometer coupled to a high-sensitivity CMOS detector, achieving a resolving power of up to 150,000. A modified hollow cathode lamp, originally developed at Imperial College London, was used to generate a stable neodymium plasma using argon as a carrier gas. We include an in-depth characterisation of our high-resolution setup, including spectral calibration, resolution assessment, instrument response function, and CMOS noise analysis. The validity of the partial local thermodynamic equilibrium (pLTE) assumption in the hollow cathode lamp was tested by measuring transition probabilities for 15 Nd II lines in the spectral range 378–521 nm. The derived transition probabilities show agreement within 30% of the reference values. This validation paves the way for accurate measurements of currently unreported Nd III transition probabilities, providing critical data for future astrophysical modelling efforts.

1. Introduction

The demand for high-precision experimental atomic data for lanthanides, particularly neodymium, is well established, given their critical role in accurate astrophysical modelling. Neodymium has been identified in several astrophysical environments [1-7], including the H-band spectra of APOGEE [1] and the recent Gaia data release [2]. Its abundance has also been reported in the solar photosphere [3], open clusters [4], a large sample of FGK stars [5], and hot chemically peculiar stars [6]. The detection of the neutron star merger GW170817 [8] and its electromagnetic counterpart AT2017gfo [9, 10] further underlined the importance of accurate atomic parameters for ionised lanthanides — such as Nd III — in modelling kilonova opacities [7,11-13]. The number of theoretical atomic structure calculations aimed at improving opacity estimates for kilonova modelling has increased in recent years [7,14-16]. However, their reliability still depends on validation by experimental measurements [17]. The lack of comprehensive and accurate experimental atomic data remains one of the main limitations to the refinement of kilonova models [7,11,14,15, 18].

Despite their astrophysical importance, experimental atomic data for the lanthanides remain scarce — mainly due to the extreme spectral complexity resulting from their open 4f subshells, which produce densely packed, line-rich spectra that require high-resolution spectroscopic setups for accurate analysis. Among these elements, doubly ionised neodymium (Nd III) is particularly under-characterised. While recent work has reported experimental energy level analyses for Nd III [19,20], reliable experimental transition probabilities (Einstein A coefficients for spontaneous emission) are still missing from major databases such as the Atomic Spectra Database (ASD) from the National Institute of Standards and Technology (NIST) [21]. Moreover, accurate experimental lifetimes, which are important for the measurement of transition probabilities using branching fractions, are scarce [22].

Our laboratory, which has provided high-precision transition probabilities for noble gases over the last three decades [23–25], aims to help fill this gap by reporting new experimental transition probability values for Nd III in future publications. As a step towards this goal, we have improved the resolving power of our experimental setup by integrating a PCO Edge 4.2 UV CMOS camera (6.5 μ m pixel size) with a 1.5 m Jobin-Yvon Czerny-Turner spectrometer equipped with

E-mail address: pratyushranjan.sen-sarma@uva.es (P.R. Sen Sarma).

^{*} Corresponding author.

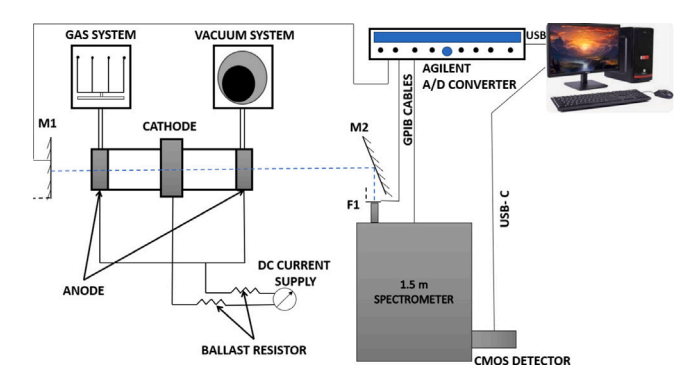


Fig. 1. Schematic representation of the experimental setup. M1, M2: plain mirror; F1: flap to block light during background measurements.

a 2400 lines/mm grating. This configuration allows the detection of spectral lines with a minimum full width at half maximum (FWHM) of approximately 4.5 pm at 632.8 nm — an improvement over previous setups that achieved 20 pm with an optical multichannel analyser (OMA) and 7 pm with an intensified CCD (ICCD). We are also using a custom-built hollow cathode lamp (HCL), based on a design developed at the Fourier Transform Spectroscopy Laboratory at Imperial College London, which has been shown to effectively produce Nd III lines for energy level studies [19,20].

This paper presents a detailed characterisation of the upgraded experimental system, including dispersion calibration, spectral resolution measurement, determination of spectral sensitivity (instrument response function) using calibrated deuterium and tungsten standard lamps, and dark-noise analysis of the CMOS detector. To assess the validity of the partial local thermodynamic equilibrium (pLTE) assumption in our custom-built hollow cathode lamp, we measured the transition probabilities of 15 prominent Nd II lines in the spectral region 378–521 nm using the Boltzmann plot method and compared them with the reliable experimental results of Den Hartog et al. 2003 [3]. If pLTE holds for Nd II, then it increases the likelihood of pLTE in Nd III under similar plasma conditions. In future work, we aim to extend this approach of transition probability measurement to Nd III, enabling the determination of transition probabilities without relying on the currently insufficient number of experimental lifetimes.

2. Experimental setup

Our experimental setup, depicted in Fig. 1, integrates three essential components: the hollow-cathode lamp as the primary plasma source, a diffraction grating spectrometer to collect the radiative emission, and the CMOS PCO Edge 4.26 UV camera to capture the emitted spectra.

Hollow-cathode emissions containing the spectral signature of the cathode material are acquired using a spectrometer paired with a CMOS detector. During spectrum acquisition, light from the lamp is reflected by mirror M2 onto the entrance slit of the spectrometer, with flap F1 in its retracted position, as indicated by the dotted lines in Fig. 1. The spectrometer isolates light of the selected wavelength — defined by its syntony, i.e., the wavelength centred on the detector — and directs it to the detector to record the spectrum. Mirror M1 is used for the reconstruction of self-absorbed spectral lines as described in [23]. The motorised components — M1, M2, F1, and the grating — are synchronised and controlled via GPIB communication using an Agilent A/D converter.

2.1. Plasma source

The plasma source used in this study, shown in Fig. 2, is a custombuilt hollow cathode lamp measuring 23 cm in length and 6.6 cm in

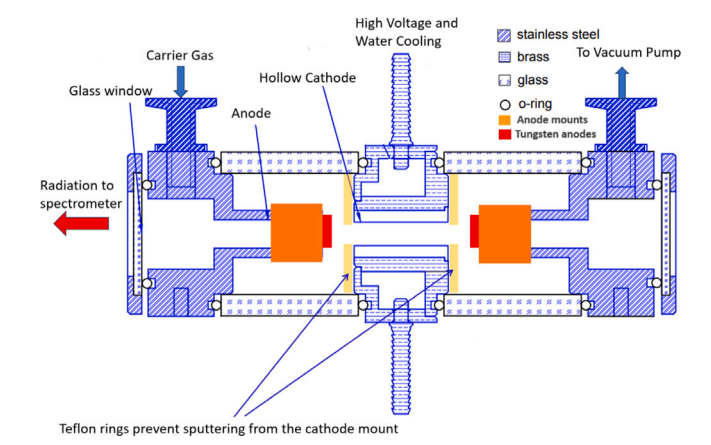


Fig. 2. Schematic diagram of the modified hollow-cathode lamp. (For interpretation of the references to colour in this figure legend, the reader is referred to the web version of this article.)

diameter. It has a symmetrical geometry with two tungsten anodes and a central cathode fitted with a replaceable hollow cylindrical insert made of the target material — in this case, neodymium. The neodymium insert has a length of 40 mm, an outer diameter of 10 mm, an inner diameter of 8 mm, and a purity of 99.9%. A DC power supply (Fug-Elektronik GmbH, 8200 Rosenheim, Germany) of up to 1 A and 2 kV in series with an 800 Ω ballast resistor ignites and maintains the plasma. The emission is collected from one end of the lamp through a 3 mm thick, 5 cm diameter fused silica window (WFS-503) with an effective light collection aperture of 3.6 cm for coupling into the spectrometer.

This lamp design originates from the Fourier Transform Spectroscopy Laboratory at Imperial College London, where it was initially developed for spectroscopic studies of iron group elements and later adapted for studies of doubly ionised neodymium (Nd III) [19,20,26–29]. The primary motivation for selecting this lamp is its demonstrated ability to produce a stable Nd III plasma, as confirmed by previous studies [19,20]. Such plasma conditions are unlikely to be reliably achieved with commercial hollow cathode lamps or alternative sources such as laser-induced breakdown spectroscopy (LIBS), which, although successful for neutral and singly ionised neodymium (Nd I, II) [3,30–32], have not provided Nd III data.

However, in its original configuration, the plasma extended beyond the hollow cylindrical cathode insert and interacted with the cathode mounts. To improve sputtering from the cathode and to better confine the discharge between the electrodes, three key modifications were made, as shown in Fig. 2: (i) stainless steel holders (orange) were added to the anodes to improve plasma confinement, (ii) tungsten rings (red) replaced the exposed stainless steel surfaces to reduce unwanted sputtering, and (iii) Teflon rings (yellow) were added to shield the cathode holders and prevent plasma interaction with non-target components. These modifications effectively concentrated the discharge energy on the cathode material, improving the stability of the lamp at higher currents.

To assess the effect of the changes in the design of the Hollow Cathode Lamp (HCL) on its discharge behaviour, we compared its operating characteristics before and after the changes. To maximise the signal-to-noise ratio in the recorded spectra, the lamp was positioned at 14 cm from the entrance slit of the monochromator so that the light entering the spectrometer corresponds to the full solid angle subtended by the cathode diameter. Before operation, the lamp is evacuated to a base pressure of 10^{-3} Pa using a Pfeifer DUO 5M rotary vacuum pump (model 35614, Asslar). Argon, used as a carrier gas, is then introduced continuously at controlled pressures ranging from 20 Pa to 200 Pa. The gas flow is controlled by an MKS Type 1179 A Mass-Flo controller, and

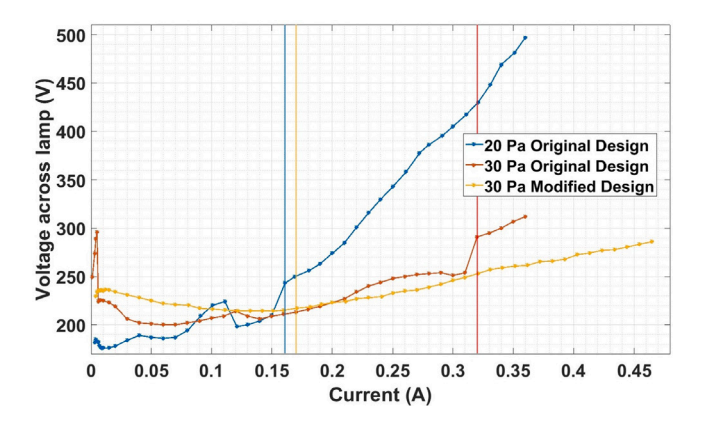


Fig. 3. Gas discharge curves comparing the modified and original lamp designs with a hollow cylindrical neodymium cathode insert. Vertical lines of matching colour indicate the discharge currents at which the transition from the normal to the abnormal glow regime occurs for each corresponding discharge curve.

an Edwards APG200 Pirani manometer monitors the operating pressure inside the hollow cathode lamp.

With the modified lamp in operation, we examined how its discharge characteristics compared with those of the original configuration. Low-pressure glow discharges are well known to offer superior spectroscopic conditions compared to arc discharges [33]. This regime is characterised by a self-sustained plasma in which the current increases linearly with voltage. In the original design using an iron cathode insert, gas discharge curves confirmed operation within this abnormal glow regime over a wide range of currents [34] and for different values of pressure inside the lamp. However, when a neodymium cathode insert was used, the discharge initially occurred in the Townsend regime—a low-current phase that is marked by the ionisation of the gas molecules by collision with electrons accelerated by the applied electric field. Transition to the abnormal glow regime occurred only at higher discharge currents, indicating that more energy input was required to achieve the same spectroscopic conditions.

This behaviour changes with the modified design. Fig. 3 compares the gas discharge curves for the modified and original lamp configurations using a neodymium cathode at 30 Pa. In addition, the discharge characteristics of the original design at 20 Pa are also included. In the original configuration, the transition from normal to abnormal glow occurred at a lower current when the pressure was reduced, consistent with the expected increase in transition current with pressure. At 30 Pa, the transition in the original design occurred at 0.32 A, while in the modified design, it occurred at a significantly lower current of 0.17 A. This lower transition current at the same pressure enables the modified lamp to operate across a wider current range within the desired discharge regime, without reaching the current limit of the power supply.

Furthermore, the modified lamp demonstrates improved plasma stability at higher currents, as evidenced by the ability to measure the discharge curve at current levels unattainable with the original configuration due to the unstable behaviour of the lamp.

2.2. Spectrometer

We use a 1.5 m Jobin-Yvon spectrometer with a square reflective diffraction grating of side 11 cm with a spatial period of 2400 lines/mm optimised for 400 nm. Fig. 4 shows the schematic diagram of it. The radiation emitted from the lamp containing spectral data from the neodymium cathode and the carrier gas is guided to the entrance slit $R_{\rm E}$ by mirror M2 from (Fig. 1). After reaching the parabolic mirror E_1 (focal length 1.5 m), it is collimated and directed to the reflective

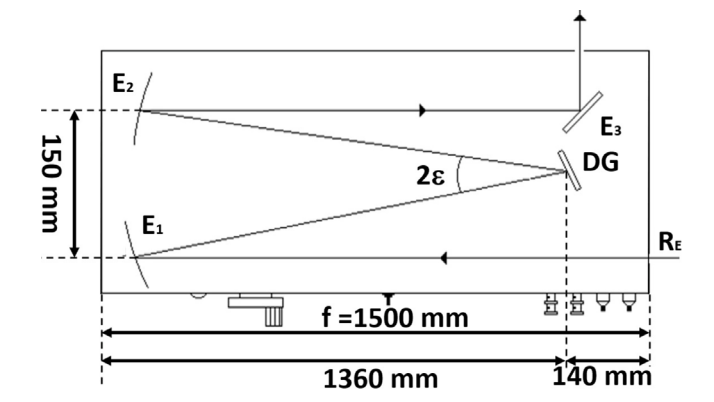


Fig. 4. Schematic diagram of the monochromator. R_E : entrance slit of the spectrometer, E_1 , E_2 : parabolic mirrors with f as focal length, DG: reflective diffraction grating, E_3 : plane mirror and ϵ : constant deviation semi-angle of the spectrometer.

grating DG. The grating isolates the light of the selected wavelength and directs it to the second parabolic mirror E_2 , which focuses it on the CMOS detector with the help of the plane mirror E_3 . The configuration used is a single-pass Czerny-Turner, providing a constant deviation angle (2 ε in Fig. 4) of 0.1102 radians. This setup covers a spectral range of 200 nm to 800 nm and offers a resolving power of up to 150,000 at 450 nm. Changing the syntony from 200 nm to 800 nm takes approximately 14 min, and the integration time to acquire and store a spectrum (spectral range ≈ 3 nm) is less than 1 s. The width of the entrance slit can be adjusted from 10 μm to 1500 μm .

2.3. Detector

In this work, we have integrated a PCO Edge 4.2 bi-USB sCMOS camera from Excelitas Technologies as the detector in our experimental setup. This highly sensitive, low-noise imaging device is optimised for precise spectral analysis. It features a 13.3 mm \times 13.3 mm backilluminated scientific CMOS (bi-sCMOS) sensor with 2048 \times 2048 active pixels, each measuring 6.5 $\mu m \times$ 6.5 μm . The sensor offers a quantum efficiency of up to 95% at 600 nm, making it ideal for low-light imaging. It covers a spectral range of 190–1100 nm, with our experiment utilising the 200–800 nm range.

An adjustable forced-air Peltier system cools the sensor, effectively minimising dark noise during long exposures. Data is transferred via a USB 3.1 Gen 1 interface, allowing high-speed data acquisition. The camera supports adjustable exposure times from 21 μs to 20 s, providing versatility for different experimental conditions.

To align the detector, a He–Ne laser was positioned in front of the spectrometer, and the syntony was set to 632.8 nm. The image of the spectrometer's entrance slit, formed by the laser light on the detector's optical sensor, was observed using the camera control software [35]. The detector was translated horizontally along the optical axis, perpendicular to the spectrometer's exit plane, to sharpen the image and achieve optimal focus. Additionally, the detector was rotated such that the horizontal border of the detector was as parallel as possible to the optical bench.

3. Image to spectra

After an image is acquired with the detector, a one-dimensional spectrum (intensity versus wavelength) is typically obtained by adding up the intensity of all the pixels in the same column. However, the spectrometer's entrance slit is not a rectangle. Monochromators operating as spectrometers work off-axis and use a curved entrance slit so that all its points are at the same distance from the optical axis

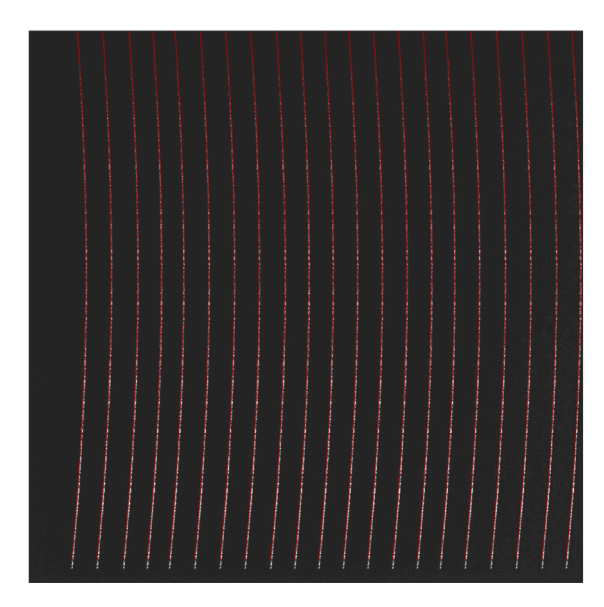


Fig. 5. Plot created by superimposing individual figures of the image of the monochromator's entrance slit falling on different positions of the detector using the 632.8 nm line of a He–Ne laser.

and therefore they will be equally affected by optical aberrations [36]. Consequently, this curvature manifests in the spectral lines formed at the monochromator's exit plane where the detector is positioned. Thus, it is important to consider the curvature of the entrance slit when converting the captured 2D image into a 1D spectrum.

To measure the curvature of the entrance slit, a He–Ne laser emitting at 632.8 nm was carefully aligned with the spectrometer, and the resulting image of the spectral line falling on the camera sensor was captured using the camera control software [35]. The monochromator was incrementally tuned in steps of 0.1 nm to scan the image of the entrance slit across the detector. Fig. 5 displays the composite image of the spectral lines acquired at different monochromator tunings. It should be noted that the figure presents a horizontal concatenation of the individual line images obtained at each tuning step. These images reveal the curvature of the spectral lines at the monochromator's exit plane, which reflects the curvature of the entrance slit. The red dots in the figure indicate the pixels with maximum row intensity for each line; these points are used to model the curvature and to ensure accurate spectral extraction from the camera images.

Two models were employed to fit the curvature of the entrance slit: circular and parabolic fits. The purpose of fitting these models is to determine which model best represents the curvature and ensures more precise spectral measurements.

Circular Fit: In this model, the curvature of the entrance slit is approximated as part of a circle. Using the row maxima from the captured images, a least-squares fitting method was applied to fit a circular arc to the observed data. The circle is described by three parameters: the radius of curvature r, and the coordinates of the centre, x_0 and y_0 . The fitting function is:

$$(x - x_0)^2 + (y - y_0)^2 = r^2$$

where x and y are the pixel coordinates of the entrance slit's image, r is the radius of curvature, x_0 and y_0 are the coordinates of the centre of the circle.

Parabolic Fit: The parabolic fit was applied using the equation:

$$y = x_v - a(x - y_v)^2$$

where a is the parabolic coefficient, and x_v and y_v represent the fitted vertex coordinates of the parabola. This equation describes how the curvature of the entrance slit is approximated as a parabolic arc. The

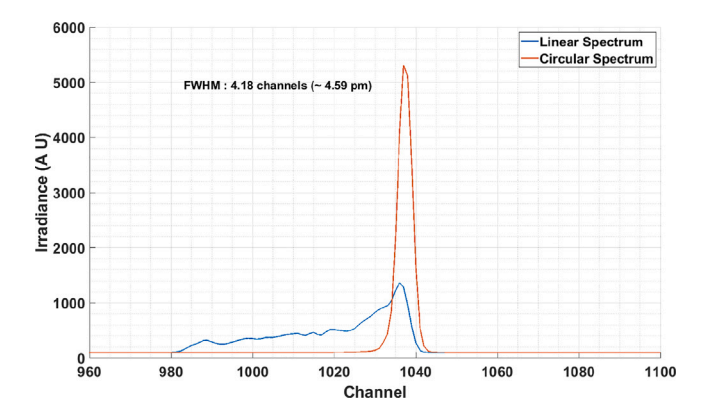


Fig. 6. Comparison of spectra for the He–Ne laser line at 632.8 nm, illustrating results obtained using the circular fit model and the linear sum.

same method as above was used for fitting and the parameters were extracted

We chose the circular model because a circular slit is practically more feasible to make than a parabolic slit, making the circular model more realistic.

By solving the circular model [36] and organising pixels according to their positions relative to the curve, we classify them into distinct channels. Each channel represents a group of pixels illuminated by light of the same wavelength. Consequently, the resulting spectrum displays irradiance on the vertical axis and channels on the horizontal axis. The intensity associated with a given channel is calculated as follows:

$$col = \lfloor x \rfloor$$

$$frac = x - col$$

$$I (channel) = \sum_{y=1}^{2048} img(col,y)*(1-frac) + img(1+col,y)*frac$$

The notation $\lfloor x \rfloor$ represents the greatest integer less than or equal to x, also known as the floor function. This method ensures that the curvature of the entrance slit is properly accounted for when generating the spectra from the image, leading to improved spectral resolution.

Ignoring the curvature of the entrance slit during spectral extraction leads to a significant degradation in spectral resolution by increasing the full width at half maximum (FWHM) of the spectral lines, causing them to become asymmetric, and also reduces the signal-to-noise ratio (SNR), introducing uncertainties in spectral analysis, particularly in the calculation of intensities of spectral lines. Fig. 6 compares spectra for the He–Ne laser line at 632.8 nm, illustrating results obtained with a circular fit and when the curvature is not taken into account. The spectrum generated using the circular model gives an FWHM of 4.18 channels or 4.59 pm (the process of converting channels to wavelength is discussed in the next section), whereas the linear sum fails to produce a well-defined line, making the FWHM meaningless.

4. Calculation of dispersion

Dispersion calibration of a spectroscopic experimental setup is critical when using a multi-channel detector. It provides an accurate understanding of the wavelength range covered by each detector channel. As previously described, our experimental setup measures in the wavelength range from 200 nm to 800 nm. Due to the use of a diffraction grating spectrometer, the nm/channel ratio varies over this range. Accurate spectral data along the wavelength axis therefore requires thorough dispersion calibration. In addition, the dispersion characteristics can vary between different detector channels, emphasising the need for a comprehensive calibration.

The dispersion calibration method involves finding the ratio of the difference in wavelength $(\lambda_2 - \lambda_1)$ of two lines whose wavelengths

 $(\lambda_1,\,\lambda_2)$ are known with high precision from [21], and the distance in channels between them in the spectrum. We have only chosen those pairs of lines whose transition probabilities are greater than $10^6~{\rm s}^{-1}$, which are separated from each other by at least 0.02 nm, but fit within 2048 channels of the detector and have high intensity as indicated in [21]. Using this approach, we measure the inverse linear dispersion for the intermediate wavelength between λ_1 and λ_2 using the following equation:

$$\frac{d\lambda}{dchannel} \left(\frac{\lambda_1 + \lambda_2}{2} \right) = \frac{\lambda_2 - \lambda_1}{\Delta channel} \tag{1}$$

where Δ channel corresponds to the difference between the centres of the spectral lines

We used a sodium (Na) spectral lamp and the in-house hollow-cathode lamp for this calibration. The spectral lamps were carefully aligned with the experimental setup and the spectrometer was tuned to the appropriate wavelengths. We measured seven doublets (six argon (Ar) and one sodium (Na)), four argon triplets, and sets of four, five, and eight argon lines, spanning a wavelength range from 200 to 800 nm [37]. All chosen lines fit within the 2048 channels of the detector. Finally, the inverse linear dispersion for each doublet was calculated using Eq. (1).

Based on the monochromator scheme provided in Fig. 4, the dispersion equation can be expressed as:

$$\frac{d\lambda}{dchannel} = \frac{\lambda c(-BE + \sqrt{1 + E^2 - B^2})}{2Bf(1 + E^2)} \tag{2}$$

with

$$E = \frac{\sin(2\epsilon)}{1 + \cos(2\epsilon)}$$

$$B = \frac{\lambda}{2d(1 + \cos(2\epsilon))}$$

where, the constant deviation semi-angle $\epsilon \approx \tan(\epsilon) = (150/2)/1360 = 0.0551 \pm 0.0005$ radians; λ is the wavelength; 2d represents the spatial period of the diffraction grating DG, which is 1/2400 lines/mm; f denotes the focal length of the monochromator's collecting mirrors (E_1 and E_2) and c denotes the width of the detector pixels. The values of f and c as specified by the manufacturers are 1500 mm and 6.5 μ m respectively, thus the calculated value of the ratio of the manufacturer given values $c/f = 4.33 \times 10^{-6}$.

However, when the experimental values of $\frac{d\lambda}{dchannel}$ from Eq. (1) are used in Eq. (2) to calculate the same ratio, the mean value is 4.38×10^{-6} . This discrepancy between the manufacturer's and experimental values arises because, in practice, f represents the distance between the collecting mirror (E_2) and the sensor of the camera, which ideally should match the focal length of E_2 . Still, the experimental measurements account for factors such as the setup's depth of focus, and pixel dimension irregularities ($\Delta c \approx \pm 0.5 ~\mu m$ as provided by the manufacturer). Fig. 7 shows how the experimental c/f changes with wavelength. The difference in the experimental values and the calculated values increases after 550 nm. This is probably due to the anti-reflective coating, which is discussed later.

We use the mean of the experimental values of $c/f=4.38\times 10^{-6}$ in Eq. (2) to derive the calculated values of inverse linear dispersion over the wavelength range of 200 nm to 800 nm. Fig. 8 presents the experimental inverse linear dispersion (obtained using Eq. (1)), shown in blue, and the calculated inverse linear dispersion (shown in red) obtained using Eq. (2) with experimental c/f values. In yellow, we present the inverse linear dispersion values calculated using the same equation with the pixel values from the previous ICCD camera (= 13.9 μ m). This plot highlights the improvement in resolution, as the dispersion value (pm/channel) for the ICCD camera was twice as large as the value obtained with the CMOS camera.

Fig. 8 shows that the inverse linear dispersion for both the present and the past setup decreases with increasing wavelength.

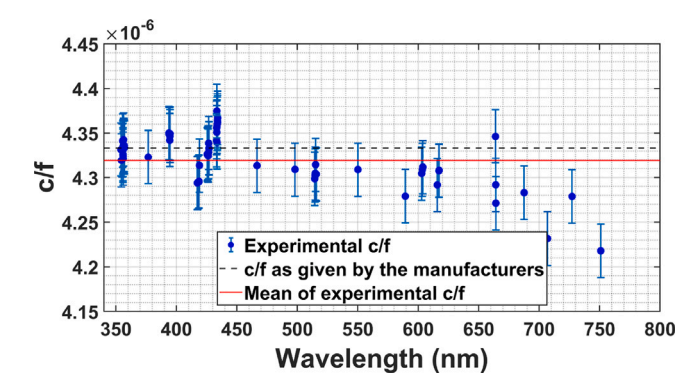


Fig. 7. Comparison of experimental c/f and the one calculated with the specifications provided by the manufacturer.

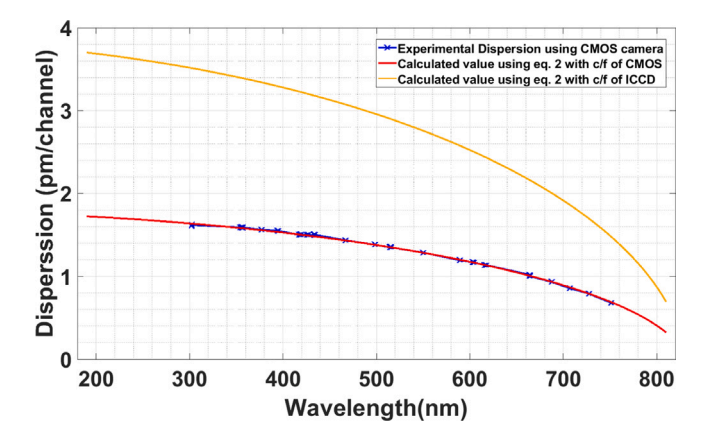


Fig. 8. Comparison of the experimental (blue) and calculated (red) inverse linear dispersion values for the CMOS camera, along with the corresponding calculated values for the ICCD camera (yellow). (For interpretation of the references to colour in this figure legend, the reader is referred to the web version of this article.)

We have also investigated the dependency of the dispersion characteristics with channels for a given wavelength. To investigate this, we recorded the Ar II lines at 726.5 nm and 727.06 nm and the Na I doublet at 588.99 nm and 589.6 nm. By changing the wavelength falling on the centre of the photodetector of the camera, we moved these lines across the detector channels. We then applied the following equation to assess the dependence of the inverse linear dispersion on the channels.

$$\frac{d\lambda}{dchannel} \left(\frac{channel_1 + channel_2}{2} \right) = \frac{\lambda_2 - \lambda_1}{\Delta channel}$$
 (3)

The values obtained from Eq. (3) for the Ar II lines were analysed to determine the mean, which was found to be equal to that obtained from Eq. (1). Similarly, for the Na I doublet, the mean of the values from Eq. (3) matched the result from Eq. (1). These results confirm that the dispersion does not depend on the detector's channel. Fig. 9 shows the dependence of the inverse linear dispersion on the channel number: the Ar II experimental data are shown in solid blue and the corresponding calculated value from Eq. (1) is shown as a dashed blue line, while the corresponding data for the Na I doublet are shown in solid red and dashed red lines, respectively.

5. Noise characterisation

Several types of noise can limit the performance of CMOS cameras, with dark noise being the most significant. Dark noise is the random signal generated in the absence of light, primarily arising from two sources: thermal noise and dark current.

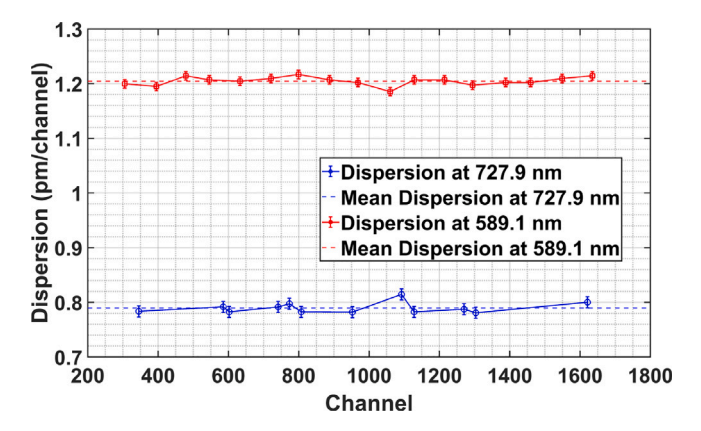


Fig. 9. Dependence of the inverse linear dispersion with the detector's channels and their mean values.

Thermal noise occurs due to the random motion of charge carriers within the semiconductor material of the sensor, which is influenced by the detector temperature [38,39]. As the temperature increases, so does thermal noise. In our setup, the PCO Edge 4.2 bi sCMOS camera is equipped with an adjustable Peltier cooling system that uses forced air (fan) to regulate the temperature and reduce thermal noise during long exposures. This system requires approximately 2 to 3 min to stabilise after the CMOS camera is powered on. Allowing the sensor to reach thermal equilibrium by operating it for a few minutes before data acquisition minimises fluctuations in thermal noise.

Dark current, by contrast, refers to the unwanted flow of current through the sensor even when no light is present, caused by thermal excitations of charge carriers. Dark current can manifest as non-uniform pixel readings across the sensor, leading to noise in the final data.

To investigate the characteristics of dark current, we captured and summed 500 dark frames (images in the absence of light) using slit widths of 25 μ m and 70 μ m, with exposure times of 50 μ s, 100 μ s, and 500 μ s. Additionally, 200 dark frames were captured and summed with a 25 μ m slit width under the same exposure conditions to explore the dependence of noise on the number of captures. Our results revealed that dark noise is independent of slit width and exposure time and is primarily influenced by the number of frames captured. This is illustrated in Fig. 10, where the *y*-axis represents measured intensity for every pixel of the detector, and the *x*-axis corresponds to pixel number (numbered from the upper left to the lower right corner, with 2048 pixels per row). The figure demonstrates dark noise for a 25 μ m slit width at exposure times of 50 μ s, for both 200 and 500 frame captures. These findings indicate that dark noise is only sensitive to the number of frames acquired rather than to other experimental parameters.

To mitigate the effects of dark noise, we employed dark frame subtraction. This technique involves capturing dark frames under the same conditions as the light frames (signal frames) and subtracting them after both have been converted from images to spectra as previously discussed. Dark frames should be captured within seconds of the light frames to minimise the effects of temperature fluctuations and spectral dependencies. This process effectively reduces dark noise, taking into account its particular spatial distribution in the final spectrum, producing cleaner, more reliable data.

Furthermore, we examined the pixel-to-pixel variation in dark noise by calculating the coefficient of variation (CV), defined as the ratio of the standard deviation to the mean. The CV of the data is 1.13%. This slight variation is attributed to a 300-count intensity reduction in the top 200 rows (409600 pixels), beyond which the intensity remains constant. Fig. 11 highlights the intensity variation across rows 505 to 515 (pixels 1034240 to 1054720), revealing a periodic distribution This behaviour is similar to the one observed in [40] since the readout architecture of PCO Edge 4.2 bi sCMOS camera is very similar to that

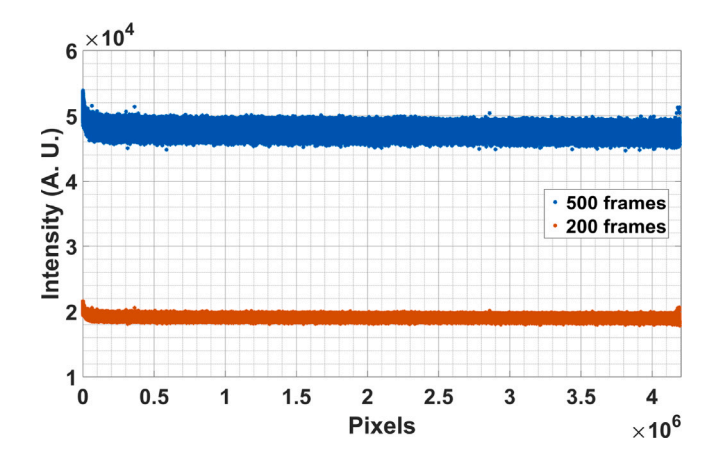


Fig. 10. Representation of dark noise for 200 and 500 accumulations in orange and blue, respectively, for an exposure time of 50 μ s.

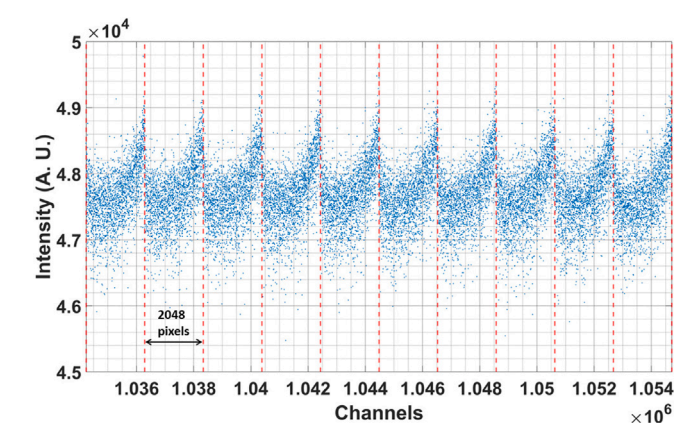


Fig. 11. Representation of dark noise obtained for 500 accumulations, exposure time of 500 μs , and a slitwidth of 25 μm from pixels 1034240 to 1054720 (rows 505 to 515). The red dotted lines represent the end of the previous row and the beginning of the next one.

of an ICCD camera as discussed in [40]. Thus this proves that, however small, there is a particular spatial distribution of the dark noise in the final image.

6. Spectral resolution

The spectral resolution of a spectrometer with a given diffraction grating is primarily determined by its entrance slit width and the pixel size of the detector. In an ideal, aberration-free spectrometer, the spectral line profile, or line spread function (LSF), arises from the convolution of the transmission functions of both the entrance slit and the detector pixels. Assuming rectangular transmission functions for both, the resulting LSF exhibits a trapezoidal shape. When the slit width matches the pixel size, the LSF simplifies to a triangular profile, as the convolution of two equal-width rectangular functions.

We use the PCO Edge 4.2 bi sCMOS camera to capture the spectrum of the 632.8 nm line from a He–Ne laser. Spectra were recorded across a range of entrance slit widths, from 5 μm to 130 μm , and exposure times from 50 μs to 1300 μs . Fig. 12 presents a comparison of the experimental LSF (in blue) and the simulated LSF (in red) for slit widths of 20 μm (left) and 40 μm (right), both measured with an exposure time of 500 μs .

The experimental and simulated LSFs show good agreement in terms of spectral width. This indicates that our theoretical model — based on slit width and detector pixel size — predicts the spectral resolution

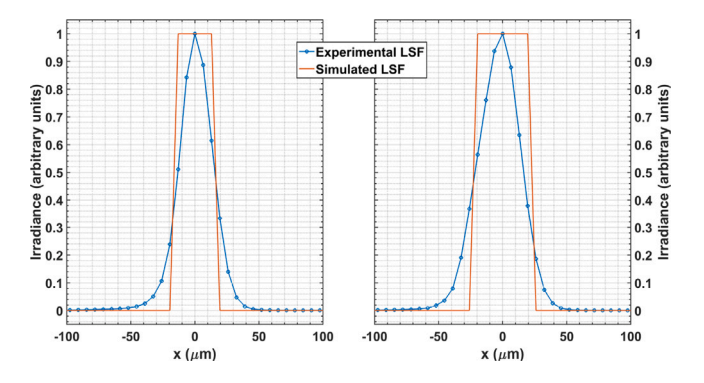


Fig. 12. Measured LSF (in blue) and simulated LSF (solid red) for 20 μ m (left) and 40 μ m (right) for an exposure time of 500 μ s. (For interpretation of the references to colour in this figure legend, the reader is referred to the web version of this article.)

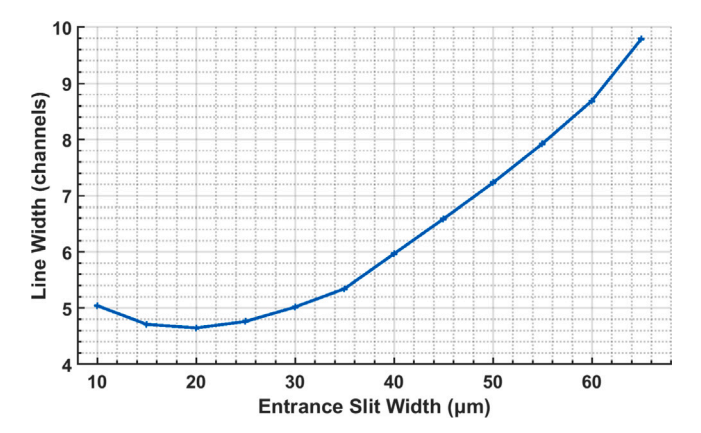


Fig. 13. Instrumental broadening in channel units as a function of the entrance slit width for an exposure time of 400 ms.

well. However, it is important to mention that the simulated LSF does not account for several factors that can influence the LSF's shape. These factors include the laser beam profile, diffraction effects from the grating, pixel crosstalk, and slight defocusing, all of which tend to smooth the LSF for larger slit widths.

In Fig. 13, the full width at half maximum (FWHM) of the experimental line spread functions (LSFs) is plotted as a function of entrance slit width for an exposure time of 400 ms. For the narrowest slit widths, the FWHM remains approximately constant, but it begins to increase almost linearly above 20 μm - indicating a critical threshold. This threshold defines the optimum entrance slit width: narrower slits reduce light throughput without improving resolution, while wider slits increase signal intensity at the expense of broader instrumental profiles. The measured FWHM of the LSF also characterises the instrumental broadening of the spectroscopic setup.

It was observed that although exposure time influences signal intensity, it does not affect the full width at half maximum (FWHM) of the line spread functions (LSFs) or the spectral resolution of the system. This confirms that, for a given detector pixel size and grating, the spectrometer's resolution is primarily governed by the entrance slit width. As shown in Fig. 13, instrumental broadening increases with slit width and becomes noticeable above approximately 20 μm . Therefore, to maximise signal intensity without compromising spectral resolution, the slit width can be safely increased up to 20 μm . For the He–Ne laser line at 632.8 nm, this configuration yields an instrumental broadening of approximately 4.5 pm corresponding to a resolving power of nearly 150,000 (R = 632.8/0.004), based on the dispersion data in Fig. 8. In comparison, the previous setup required a minimum usable slit width

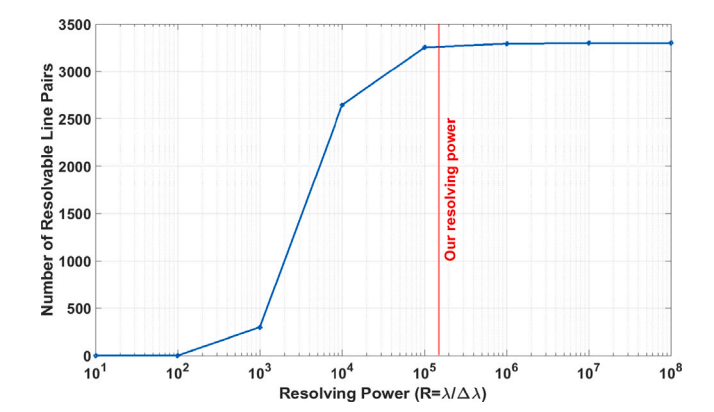


Fig. 14. Number of resolvable line pairs vs instrumental width.

of 35 μ m, resulting in an instrumental broadening of about 7 pm at the same wavelength, corresponding to a resolving power of nearly 76,000. This demonstrates a significant improvement in spectral resolution with the upgraded system.

This narrow instrumental width is crucial for the accurate measurement of the transition probabilities of Nd III, as our lamp — designed according to the configuration used in [19,20] — produces emission lines from several species, including Ar I, Ar II, Ar III, Nd I, Nd II and Nd III. According to the identified line lists available from the NIST Atomic Spectra Database [21] (for Ar I, Ar II, Ar III, Nd I, and Nd II) and from [19,20] (for Nd III), a total of 3,389 spectral lines or 3388 consecutive line pairs are expected across these species within 200 nm to 800 nm.

To assess the ability of our setup to resolve the identified spectral lines present in our emission spectra, we calculated the number of line pairs that could be resolved at different resolving powers. We calculated the minimum resolving power required to resolve each successive line pair using $R = \lambda/\Delta\lambda$ ($\Delta\lambda$ is the spacing between the successive lines and λ is the wavelength) and determined how many would be resolvable above different resolving power thresholds. The results, shown in Fig. 14, indicate that with the maximum resolving power attained by our setup, more than 3254 of the 3388 identified line pairs can be resolved.

It should be noted that Fig. 14 suggests that, given the resolving power of our setup, all identified spectral lines from various species present in the hollow cathode plasma could be fully resolved. However, as highlighted in [19,20], only a fraction of the observed Nd III lines have been identified and reported. This means that the actual distance between two consecutive spectral lines in our spectra will be smaller than the estimated distance obtained using the identified lines. This highlights one of the major challenges of measuring the transition probabilities of doubly ionised neodymium: the large number of unidentified lines and the existence of line blends.

7. Response function

Accurate determination of transition probabilities requires precise measurement of irradiance ratios. To obtain accurate irradiance values — or, equivalently, the area under spectral lines — a thorough understanding of the spectral sensitivity of the experimental setup is essential. The sensitivity is primarily governed by the detector and monochromator components, which together define the system's overall response. Therefore, the response function of the setup must be characterised across the relevant spectral range and detector channels. This characterisation accounts for all factors influencing the system's response, including grating efficiency and the transmission properties of the monochromator's optical elements and the spectral response of the detector's photocathode material.

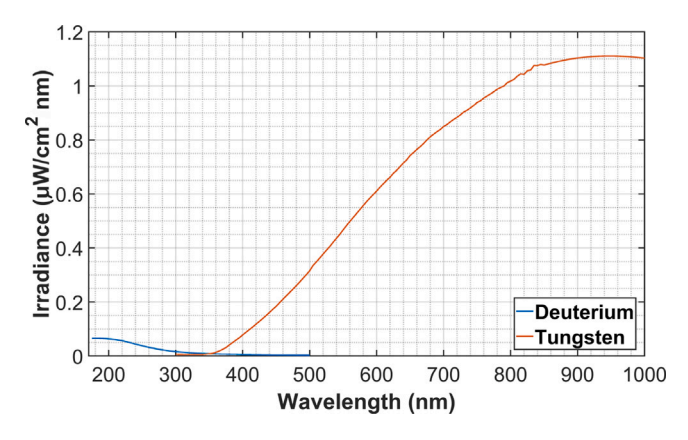


Fig. 15. Emission characteristics of the deuterium and the tungsten lamps as provided in the calibration certificates.

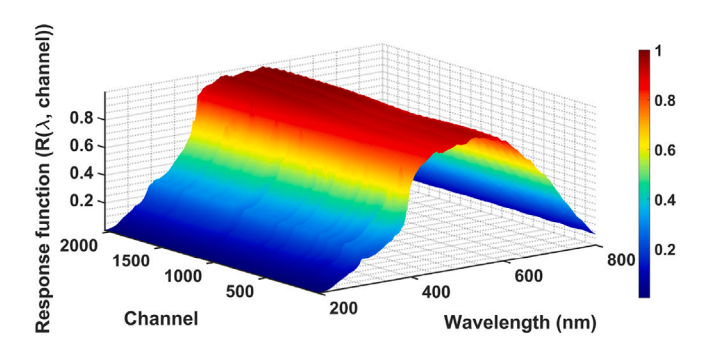


Fig. 16. 3D representation of the normalised response function $R(\lambda, \text{ch})$.

Two calibrated lamps, an L2D2 Hamamatsu deuterium lamp (model: L6566), calibrated by the manufacturer (within the range of 200–380 nm), and an FEL QHT Osram tungsten lamp calibrated against another incandescent lamp calibrated at NIST (for the spectral range of 370–800 nm) were used for this purpose. Fig. 15 shows the irradiance emission characteristics as provided in the calibration certificates, $I_{\rm D}(\lambda)$ shown in blue for the deuterium lamp and $I_{\rm W}(\lambda)$ shown in red for the tungsten lamp.

The calibration lamps were placed in place of the hollow-cathode lamp so that the distance between the hollow-cathode lamp and the monochromator was equal to that of the calibration lamp and the monochromator. Once the lamps are correctly aligned, spectra are captured by tuning the monochromator in 5 nm increments from 200 to 370 nm for the deuterium lamp and 10 nm increments from 350 to 800 nm for the tungsten lamp. Background measurements are taken after each measurement to subtract the luminous background and the dark noise of the detector from each acquired spectrum, and finally, the detected irradiance $I_d(\lambda, \operatorname{ch})$ is obtained.

The response function $R(\lambda, \operatorname{ch})$ is then calculated using the following equations:

$$R(\lambda, \text{ch}) = \begin{cases} C_{\text{D}} \frac{I_d(\lambda, \text{ch})}{I_{\text{D}}(\lambda)} & 200 \le \lambda \le 380 \,\text{nm} \\ C_{\text{W}} \frac{I_d(\lambda, \text{ch})}{I_{\text{W}}(\lambda)} & 370 \le \lambda \le 800 \,\text{nm} \end{cases}$$
(4)

where $C_{\rm D}$ and $C_{\rm W}$ are constants used to equalise the response function in the overlapping region (370 nm–380 nm).

Fig. 16 shows the global representation of the normalised analytical response function $R(\lambda, \text{ch})$.

After processing the measurements, there are 76 data sets (covering the range 200–800 nm with the specified increments) of 2048 points each, describing the function $R(\lambda, \text{ch})$. To determine the value of the

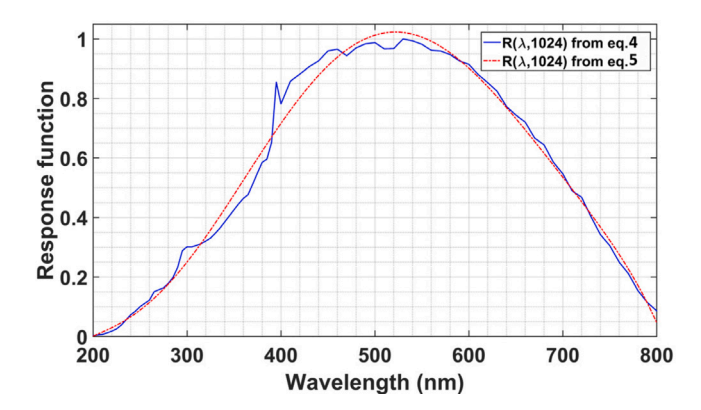


Fig. 17. Representation of the response function versus wavelength for channel 1024 of the detector.

response function for any wavelength and channel, the data points are fitted to an analytical function described by the equation:

$$R(\lambda, \text{ch}) = \sum_{i=0}^{n_i} a_i \lambda^i + \sum_{j=1}^{n_j} b_j (\text{channel})^j$$

$$+ \sum_{k_1 + k_2 = 2}^{n_k} c_{k_1 k_2} \lambda^{k_2} (\text{channel})^{k_1}$$
(5)

where a_i , b_j , and $c_{k_1k_2}$ are real numbers, and k_1 and k_2 are natural numbers. Once the adjustment is made, the values of the variables a_i , b_j , and c_{k_1,k_2} are obtained, which allows for the value of the response function to be calculated for each wavelength and each channel. A representation of the normalised value of the response function at channel 1024 and its fit is shown in Fig. 17.

We observed oscillations in the spectra at higher wavelengths during the response function measurements. Fig. 18 represents the dependence of the response function on channels for different values of wavelength syntony within the range of 400 nm to 800 nm. An oscillation in the values of $R(\lambda, \text{ch})$ is observed from $\lambda = 550$ nm, and the distance between two consecutive maxima increases with wavelength until $\lambda = 800$ nm.

As discussed earlier (Fig. 7), the experimental c/f values begin to diverge noticeably beyond 550 nm, where oscillations in the response function also appear. We traced this effect to a flat window placed in front of the CMOS sensor, which the manufacturer confirmed to have an anti-reflective coating optimised for wavelengths above 250 nm. This window introduced interference effects, causing discrepancies of approximately 2% in c/f values and up to 4% in spectral intensity measurements. Simulations of thin-film interference with non-parallel surfaces showed that the oscillations depend on the layer's thickness, the tilt angle of the surface, and the material's refractive index. To minimise these artefacts and reduce measurement uncertainty, the camera has been sent back to the manufacturer for window removal.

8. Measurement of Nd II transition probabilities for spectroscopic validation

In atomic spectroscopy, there are two widely used methods for the experimental determination of transition probabilities (Einstein A coefficients), each with specific advantages and limitations depending on the plasma source used and the objectives of the study.

The first method is based on the assumption of local thermodynamic equilibrium (LTE), in which the populations at the atomic upper energy levels follow the Boltzmann distribution. By determining the plasma population temperature and measuring relative line intensities,

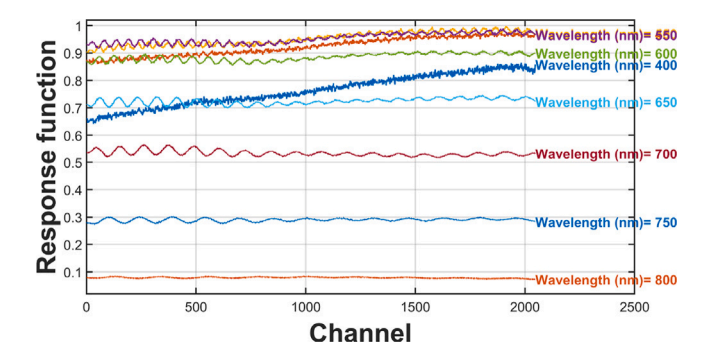


Fig. 18. Representation of the response function versus channel for different wavelengths between 400 nm and 800 nm.

transition probabilities can be inferred without the need for radiative lifetime data [23,24]. This approach is experimentally straightforward, but it requires reliable A-values for a set of reference lines to construct a Boltzmann plot and obtain the plasma population temperature. The Boltzmann method has recently been used to measure the transition probabilities of neutral and singly ionised neodymium in studies such as [30–32]. The studies in question used plasmas generated by either laser-induced breakdown (LIBS) or commercial hollow cathode lamps operated at very low currents (a few mA) as a plasma source.

The second method circumvents the LTE assumption by combining branching fraction measurements with independently determined lifetimes of the upper energy level. A branching fraction is defined as the ratio of the intensity of a line to the total intensity of all transitions from the same upper level. When multiplied by the inverse of the upper level's radiative lifetime, it gives the absolute transition probability. The advantage of this technique is that it is independent of plasma conditions or pre-existing A-values, making it applicable in non-LTE environments. However, accurate lifetime measurements are required, often obtained using techniques such as time-resolved laser-induced fluorescence (TR-LIF) [22,41], which can be challenging, particularly for high energy levels. In addition, accurate branching fraction determination requires the detection of all decay channels, some of which may lie outside the observable spectral range or suffer from line blending. The Nd II transition probabilities from Den Hartog et al. [3] were obtained using this method, which combined branching fractions from Fourier transform spectra (FTS) obtained with a commercial hollow cathode with measured lifetimes.

It is important to note that neither LIBS nor commercial hollow cathode lamps operated at low currents can produce doubly ionised neodymium (Nd III). Therefore, the use of a custom-built hollow cathode lamp capable of operating at currents up to 1 A is essential for obtaining transition probabilities of Nd III. To assess whether this source is suitable for transition probability measurements using the Boltzmann plot method (as applied in Ferrara et al. [30], Irvine et al. [32], and Ryder et al. [31]), it is first necessary to establish the validity of partial local thermodynamic equilibrium (pLTE) in the lamp. The presence of pLTE is expected to be more likely in our lamp than in conventional commercial hollow cathode lamps, as operation at currents up to 1 A enhances collisional processes and promotes better thermalisation of the energy levels as opposed to a few mA. To test this assumption, we selected 15 strong Nd II transitions and determined their transition probabilities using the Boltzmann plot method. These results were then compared with reliable experimental values reported by Den Hartog et al. 2003 [3]. This agreement serves as a validation of the pLTE assumption for Nd II in our lamp.

The selected set of 15 Nd II spectral lines is from Table 5 of Den Hartog et al. [3], based on their high-accuracy transition probabilities (NIST accuracy grades of B or better), $\log(gf)$ values within ± 1 (signifying strong transitions), and the presence of sufficient intensity in spectra measured with our setup.

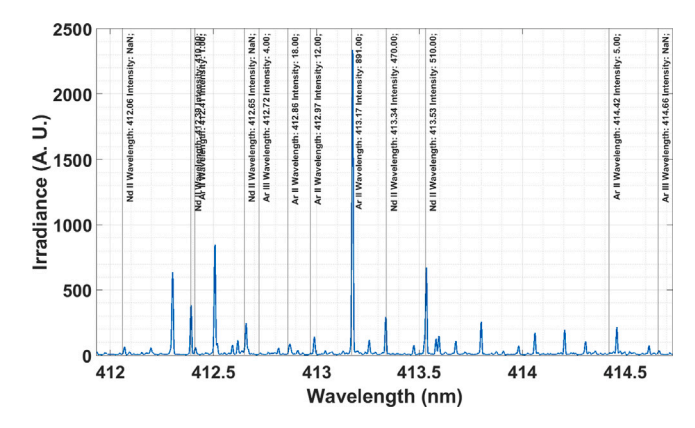


Fig. 19. The recorded spectrum exhibits emission lines corresponding to Ar I, Ar II, Ar III, and Nd II present around \pm 1.5 nm of the Nd II line of interest at 413.5 nm.

The corresponding spectra were recorded using the CMOS camera by tuning the spectrometer to each selected wavelength region. The discharge in the lamp was maintained at a current of 450 mA, a voltage of 729 V, and at a constant pressure of 30 Pa. The spectra were recorded with an exposure time of $0.2 \, \text{s}$, a slit width of $25 \, \mu \text{m}$.

Line identification was performed by superimposing reference wavelengths from the NIST Atomic Spectra Database [21] for Nd I, Nd II, Ar I, Ar II, and Ar III, along with Nd III lines reported by [19,20], onto the experimental spectra. The reference lines were horizontally shifted to align with the observed peaks. The horizontal axis of each spectrum was then converted from detector channels to physical wavelengths (in nm) using the known dispersion of the spectrometer. An example of the spectrum following the line identification procedure is shown in Fig. 19. The primary interest in this spectrum is the Nd II line at 413.55 nm Den Hartog et al. [3]. The corresponding wavelength and intensity values on the vertical lines were obtained from the NIST Atomic Spectra Database [21].

For each of the 15 target wavelengths, a spectral segment spanning ±200 channels (corresponding to approximately 0.6–0.8 nm, depending on the dispersion value) was extracted from the recorded data. The intensity of each segment was corrected using the calibrated response function of the system. As the main broadening mechanism in the hollow cathode lamp is Doppler broadening, the extracted spectra were fitted using a multi-Gaussian model combined with a linear background. The fitting model included the amplitude, centre, and width for each Gaussian component, along with parameters for the background slope and intercept. An example of the extracted and fitted spectrum corresponding to Fig. 19 is shown in Fig. 20. The irradiance values shown in Fig. 20 were obtained after the values in Fig. 19 were corrected using the calibrated spectral response function. This targeted extraction approach was adopted to reduce computational time and facilitate efficient processing of the spectra.

To ensure that the selected lines were free from blends from reported or unreported lines, the following criteria were applied:

- The R^2 value of the Gaussian fit was inspected. Lines with R^2 < 0.98 were excluded from the analysis.
- The fitted Gaussian widths were plotted as a function of wavelength. These widths oscillated around a nearly constant value of ~5 pm. Lines with widths outside the range of 4–6 pm were discarded.
- In the case of an undetected blend, the measured line intensity
 would be artificially enhanced, leading to deviations from pLTE
 conditions. In the Boltzmann Plot, this would appear as points
 lying far from the main cluster, and such lines were therefore
 excluded.

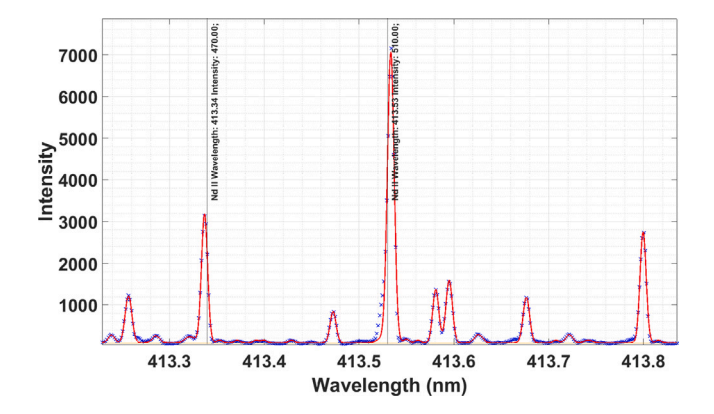


Fig. 20. This shows the extracted spectrum centred around 413.53 nm from Fig. 19, with a window of ± 200 data points. The blue crosses are he experimental data, the red are the fitted multi-gaussian model. (For interpretation of the references to colour in this figure legend, the reader is referred to the web version of this article.)

The intensity of these 15 lines was determined by calculating the area of the fitted Gaussian and was subjected to uncertainty analysis using the propagation framework developed by [25]. The uncertainty in the intensity accounts for the closeness of the neighbouring lines, blending, and the residuals of the spectral fit, i.e., the uncertainties increase if the lines are blended, close to each other, or if the model chosen for spectral fitting (a gaussian in this case) is not good enough.

Once the line intensities were obtained, we used the program *TProb.py* developed in our laboratory to calculate the transition probabilities of the 15 Nd II lines of interest, together with their uncertainties. The programme is freely available in [42] and a detailed description containing all the mathematical expressions can be found in [25]. The measured intensity values (I) were used to fit Eq. (6), where λ is the wavelength, g_u is the statistical weight of the upper level, $A_{\rm ref}$ is the reference transition probability from Den Hartog et al. [3], and E_u is the upper energy level obtained from ASD NIST [21]. The parameters b and c were determined by fitting the data to the following expression:

$$\frac{\lambda I}{g_u A_{\text{ref}}} = \exp\left(c + bE_u\right) \tag{6}$$

This method, unlike the traditional Boltzmann plot approach, which involves a logarithmic transformation, retains the original scale of the data and is less affected by points that deviate from the general trend [25]. However, it still assumes that the plasma is in local thermodynamic equilibrium (LTE), at least among the upper energy levels considered.

Once the parameters b and c were obtained from the exponential fitting, the experimental transition probability (A_{exp}) was recalculated by rearranging Eq. (6) as:

$$A_{exp} = \frac{\lambda I}{g_u \exp\left(c + bE_u\right)} \tag{7}$$

The uncertainty in the experimentally determined transition probability values (unc_{exp}) was estimated by propagating the uncertainty associated with the intensity measurements using a covariance matrix approach, incorporating correlations between the peak and width parameters to obtain $\operatorname{unc}_{A_{\operatorname{exp}}}$.

This was then combined in quadrature with the uncertainties in the reference transition probabilities (unc_{Aref}) provided by [3]:

$$unc_{exp} = \sqrt{unc_{A_{exp}}^2 + unc_{Aref}^2}$$
 (8)

This combined uncertainty accounts for various factors, including the assumption of local thermodynamic equilibrium (LTE), possible

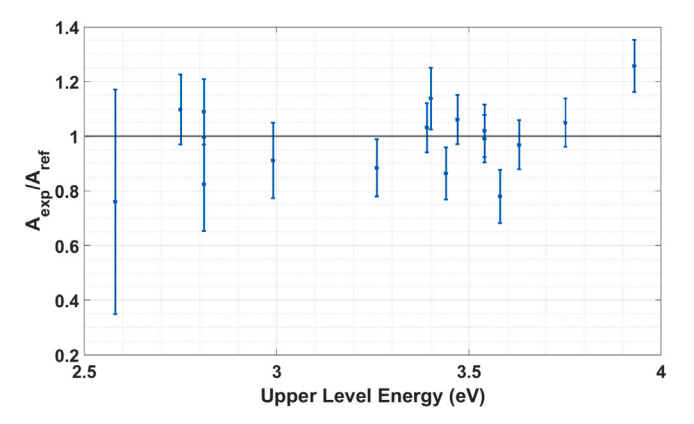


Fig. 21. Ratio of our experimentally determined transition probabilities to the reference values from Den Hartog et al. [3] shown against the upper energy levels.

misidentification of spectral lines (which may lead to incorrect intensity values and significantly impact the fit), and the propagation of uncertainties from the reference values used in Eq. (6).

The 15 Nd II spectral lines analysed in this study are included in Table 1. For each line, the table consists of: wavelength (in nm, from [3]), upper and lower energy levels (in eV, from [21]), statistical weights of the levels (from [21]), both our measured transition probabilities and those used as reference from [3], associated uncertainties, and the relative deviation of the measured values from the reference data. The recalculated transition probabilities show agreement within 30% of the published values reported in [3].

Fig. 21 plots the ratio of our experimentally determined transition probabilities to the reference values [3] as a function of the upper energy level of the transitions. The error bars represent the propagated uncertainties in the experimental transition probability values. A general decreasing trend in uncertainty is observed with increasing upper energy level (E_u), consistent with expectations under the local thermodynamic equilibrium (LTE) assumption. Higher energy levels are typically better thermalised in LTE conditions, leading to lower uncertainty in the derived transition probabilities.

The comparison of recalculated A-values obtained using our method with those reported by Den Hartog et al. 2003 [3] demonstrates the robustness of both our experiment and data-processing pipeline in producing high-quality atomic data. Moreover, it supports the applicability of the pLTE assumption in our lamp for Nd II. Although this does not directly confirm the assumption for Nd III, we reasonably assume that, since Nd III energy levels lie above those of Nd II and are therefore more likely to be thermalised, the presence of pLTE is even more plausible. This suggests that our method of measurement of A-values can be extended to Nd III in future work, particularly for prominent lines where reliable experimental lifetime values are not available. Finally, this analysis provides a stringent test of our newly developed approach for calculating transition probabilities and their associated uncertainties [25,42], applied here to a spectrum with particularly high line density.

It is worth noting that the recorded spectra shown in Figs. 19 and 20 contain several unidentified lines within narrow spectral windows of less than 3 nm and 0.6 nm, respectively, making line identification particularly challenging. Since the spectroscopic properties of argon are well documented [21,43–47], these unidentified features are more likely to be from neodymium. This underscores the need for continued high-resolution spectroscopic studies of neodymium to expand the atomic databases, improve the accuracy of line identification, and reduce the uncertainties in transition probability measurements due to line misassignment.

Table 1 Comparison of our newly measured transition probabilities of Nd II lines, $A_{\rm exp}$, with those used as a reference from Den Hartog et. al.[3], $A_{\rm ref}$. Wavelengths are taken from Den Hartog et al. 2003 [3]. The values of the upper and lower energy levels, along with their respective statistical weights, are obtained from NIST [21]. The uncertainties in the experimental and reference transition probabilities are given as percentages in brackets (= $\frac{u\pi c_A*100}{A}$ %).

λ (nm)	E_u (eV)	g_u	E_l (eV)	g_l	$A_{\rm exp}*10^6s^{-1}$	$A_{\rm ref}*10^6s^{-1}$	$\frac{A_{\rm exp} - A_{\rm ref}}{A_{\rm ref}} * 100 (\%)$
378.03	3.75	18	0.47	16	12.17 (7)	11.60 (5)	24
389.15	3.93	18	0.74	16	22.37 (8)	17.80 (5)	10
392.09	3.54	14	0.38	12	31.49 (7)	31.80 (5)	9
399.01	3.58	16	0.47	16	27.82 (8)	35.70 (5)	18
402.13	3.40	16	0.32	14	23.54 (8)	20.70 (8)	9
404.10	3.54	16	0.47	16	7.75 (7)	7.60 (6)	12
404.35	3.39	14	0.32	14	5.87 (7)	5.70 (5)	3
405.11	3.44	14	0.38	12	12.52 (8)	14.50 (5)	14
405.99	3.26	12	0.2	10	9.10 (9)	10.30 (6)	14
413.53	3.63	16	0.6	18	20.12 (7)	20.80 (5)	6
423.23	2.99	12	0.06	10	9.56 (13)	10.50 (5)	2
454.26	3.47	18	0.74	16	10.07 (8)	9.50 (5)	1
470.97	2.81	12	0.18	12	2.94 (11)	2.70 (5)	22
482.54	2.75	10	0.18	12	11.85 (12)	10.80 (5)	3
509.27	2.81	12	0.38	12	4.35 (16)	5.29 (5)	5
521.23	2.58	8	0.2	10	2.58 (41)	3.40 (5)	26

9. Conclusion

The demand for atomic data in astrophysical research is growing rapidly with the increasing volume of observations from new space-based and ground-based observatories. The substantial investment in the development of these facilities can only be justified if this demand is met with high-quality experimental atomic data, carefully measured under controlled conditions to analyse the astronomical spectra obtained. In this study, we have listed out the steps taken to ensure the accuracy of the results of our experimental measurements.

We have successfully integrated a 6.5 μm pixel size CMOS camera into our high-resolution spectroscopic system. The methodology included dispersion calibration, curvature correction, spectral resolution assessment, characterisation of the instrument response function, and dark noise analysis of the CMOS detector. We also modified the original design of our hollow cathode lamp to better confine the discharge between the electrodes, resulting in a more stable emission plasma at higher discharge currents. These improvements ensure that the setup operates at its maximum resolving power, with an upper limit of around 150,000.

The Boltzmann plot method was employed to measure the transition probabilities for 15 strong Nd II lines. Our findings agreed within 30% with the data of Den Hartog et al. (2003) [3], confirming the validity of the Partial Local Thermodynamic Equilibrium (pLTE) assumption for Nd II in our lamp. The high operating currents (up to 1 A) of our custom lamp enhance the population density of energy levels through increased collisional excitation. Because Nd III's energy levels are higher lying than those of Nd II, they are more readily thermalised under these conditions, making the pLTE assumption for Nd III even more robust. Consequently, we can confidently extend the pLTE conditions to Nd III and apply the Boltzmann plot method, detailed elsewhere in this paper, for its transition probability calculations. This capability is crucial, given the present lack of reliable experimental lifetimes for Nd III, which are essential for determining the transition probability via branching fraction measurements.

CRediT authorship contribution statement

Pratyush Ranjan Sen Sarma: Writing – original draft, Software, Investigation, Formal analysis, Conceptualization. **Maria Teresa Belmonte:** Writing – review & editing, Conceptualization, Investigation, Supervision, Validation, Resources, Funding acquisition. **Sara Llorente:** Investigation. **Santiago Mar:** Writing – review & editing, Conceptualization, Investigation, Validation.

Declaration of competing interest

The authors declare that they have no known competing financial interests or personal relationships that could have appeared to influence the work reported in this paper.

Acknowledgements

This work was conducted under the Spanish government through project PID2021-127786NA-100 funded by MICIU/AEI /10.13039/501 100011033 and by FEDER, UE. Pratyush Ranjan Sen Sarma thanks the University of Valladolid for his PhD grant. Maria Teresa Belmonte acknowledges the Beatriz Galindo Fellowship from the Ministerio de Ciencia, Innovación y Universidades of the Spanish Government. We would like to thank Augustín Martín Rodríguez for his work and support with the experimental setup and fabrication of the hollow-cathode lamp.

Data availability

The data used in this study is available on request from the corresponding author.

References

- [1] S. Hasselquist, M. Shetrone, K. Cunha, V.V. Smith, J. Holtzman, J.E. Lawler, C.A. Prieto, T.C. Beers, D. Chojnowski, J.G. Fernández-Trincado, et al., Identification of neodymium in the apogee H-band spectra, Astrophys. J. 833 (1) (2016) 81.
- [2] A. Recio-Blanco, P. De Laverny, P.A. Palicio, G. Kordopatis, M.A. Álvarez, M. Schultheis, G. Contursi, H. Zhao, G.T. Elipe, C. Ordenovic, et al., Gaia data release 3-analysis of RVS spectra using the general stellar parametriser from spectroscopy, Astron. Astrophys. 674 (2023) A29.
- [3] E.A. Den Hartog, J.E. Lawler, C. Sneden, J.J. Cowan, Improved laboratory transition probabilities for Nd II and application to the neodymium abundances of the sun and three metal-poor stars, Astrophys. J. Suppl. Ser. 148 (2) (2003) 543–566.
- [4] R. Carrera, E. Pancino, Chemical abundance analysis of the open clusters Berkeley 32, NGC 752, hyades, and praesepe, Astron. Astrophys. 535 (2011) A30
- [5] E.D. Mena, M. Tsantaki, V.Z. Adibekyan, S.G. Sousa, N.C. Santos, J.I.G. Hernández, G. Israelian, Chemical abundances of 1111 FGK stars from the HARPS GTO planet search program-II. Cu, Zn, Sr, Y, Zr, Ba, Ce, Nd, and Eu, Astron. Astrophys. 606 (2017) A94.
- [6] C.R. Cowley, T. Ryabchikova, F. Kupka, D.J. Bord, G. Mathys, W.P. Bidelman, Abundances in Przybylski's star, Mon. Not. R. Astron. Soc. 317 (2) (2000) 200–200
- [7] D. Kasen, N. Badnell, J. Barnes, Opacities and spectra of the r-process ejecta from neutron star mergers, Astrophys. J. 774 (1) (2013) 25.

- [8] B.P. Abbott, R. Abbott, T. Abbott, F. Acernese, K. Ackley, C. Adams, T. Adams, P. Addesso, R.X. Adhikari, V.B. Adya, et al., GW170817: observation of gravitational waves from a binary neutron star inspiral, Phys. Rev. Lett. 119 (16) (2017) 161101
- [9] S. Valenti, J. David, S. Yang, E. Cappellaro, L. Tartaglia, A. Corsi, S.W. Jha, D.E. Reichart, J. Haislip, V. Kouprianov, The discovery of the electromagnetic counterpart of GW170817: kilonova AT 2017gfo/DLT17ck, Astrophys. J. Lett. 848 (2) (2017) 1.24.
- [10] D. Coulter, R. Foley, C. Kilpatrick, M. Drout, A. Piro, B. Shappee, M. Siebert, J. Simon, N. Ulloa, D. Kasen, et al., Swope supernova survey 2017a (SSS17a), the optical counterpart to a gravitational wave source, Science 358 (6370) (2017) 1556–1558.
- [11] M. Tanaka, K. Hotokezaka, Radiative transfer simulations of neutron star merger ejecta, Astrophys. J. 775 (2) (2013) 113.
- [12] S. Smartt, T.-W. Chen, A. Jerkstrand, M. Coughlin, E. Kankare, S. Sim, M. Fraser, C. Inserra, K. Maguire, K. Chambers, et al., A kilonova as the electromagnetic counterpart to a gravitational-wave source, Nature 551 (7678) (2017) 75–79.
- [13] M. Tanaka, D. Kato, G. Gaigalas, P. Rynkun, L. Radžiūtė, S. Wanajo, Y. Sekiguchi, N. Nakamura, H. Tanuma, I. Murakami, et al., Properties of kilonovae from dynamical and post-merger ejecta of neutron star mergers, Astrophys. J. 852 (2) (2018) 109.
- [14] L. Maison, P. Palmeri, P. Quinet, Calculation of forbidden transitions in doubly ionized neodymium (Nd III) of interest for kilonova nebular phase analysis, J. Phys. B: At. Mol. Opt. Phys. 57 (10) (2024) 105002.
- [15] R.F. Silva, J.M. Sampaio, P. Amaro, A. Flörs, G. Martínez-Pinedo, J.P. Marques, Structure calculations in Nd III and U III relevant for kilonovae modelling, Atoms 10 (1) (2022) 18.
- [16] M. Tanaka, D. Kato, G. Gaigalas, K. Kawaguchi, Systematic opacity calculations for kilonovae, Mon. Not. R. Astron. Soc. 496 (2) (2020) 1369–1392.
- [17] G. Nave, P. Barklem, M.T. Belmonte, N. Brickhouse, P. Butler, F. Cashman, M. Chatzikos, C.R. Cowley, E. Den Hartog, S. Federman, et al., Atomic data for astrophysics: Needs and challenges, Bull. AAS 51 (7) (2019) 9.
- [18] S. Banerjee, M. Tanaka, D. Kato, G. Gaigalas, K. Kawaguchi, N. Domoto, Opacity of the highly ionized lanthanides and the effect on the early kilonova, Astrophys. J. 934 (2) (2022) 117.
- [19] M. Ding, A. Ryabtsev, E. Kononov, T. Ryabchikova, C. Clear, F. Concepcion, J. Pickering, Spectrum and energy levels of the low-lying configurations of Nd III, Astron. Astrophys. 684 (2024) A149.
- [20] M. Ding, A. Ryabtsev, E. Kononov, T. Ryabchikova, J. Pickering, Spectrum and energy levels of the high-lying singly excited configurations of Nd III-new Nd III experimental energy levels and wavelengths, with transition probability and ionisation energy calculations, Astron. Astrophys. 692 (2024) A33.
- [21] A. Kramida, Y. Ralchenko, J. Reader, NIST ASD Team, Nist atomic spectra database (ver. 5.12), 2024, [Online]. Available: https://physics.nist.gov/asd [2025, April 23]. National Institute of Standards and Technology, Gaithersburg, MD
- [22] Z.G. Zhang, S. Svanberg, P. Palmeri, P. Quinet, E. Biémont, Measurement of lifetimes by laser-induced fluorescence and determination of transition probabilities of astrophysical interest in Nd III, Astron. Astrophys. 385 (2) (2002) 724–732.
- [23] M.T. Belmonte, Experimental Transition Probabilities and Stark Parameters of Singly Ionized Noble Gases (Ph.D. thesis), University of Valladolid, 2016.
- [24] M.T. Belmonte, S. Djurović, R.J. Peláez, J.A. Aparicio, S. Mar, Improved and expanded measurements of transition probabilities in UV Ar II spectral lines, Mon. Not. R. Astron. Soc. 445 (4) (2014) 3345–3351.
- [25] M.T. Belmonte, S. Mar, S. Djurović, J.A. Menéndez, L. Gavanski, Experimental transition probabilities and oscillator strengths of singly ionised xenon (Xe II) in the ultraviolet. A fully statistical approach to the determination of uncertainties, Spectrochim. Acta Part B: At. Spectrosc. (2025) 107190.

- [26] M.T. Belmonte, J.C. Pickering, M.P. Ruffoni, E.A. Den Hartog, J.E. Lawler, A. Guzman, U. Heiter, Fe I oscillator strengths for transitions from high-lying odd-parity levels, Astrophys. J. 848 (2) (2017) 125.
- [27] C. Clear, The Spectrum and Term Analysis of Singly Ionised Nickel (Ph.D. thesis), Imperial College London, 2018.
- [28] J.C. Pickering, Measurements of the hyperfine structure of atomic energy levels in Co I, Astrophys. J. Suppl. Ser. 107 (2) (1996) 811.
- [29] C.P. Clear, J.C. Pickering, G. Nave, P. Uylings, T. Raassen, Wavelengths and energy levels of singly ionized nickel (Ni II) measured using Fourier transform spectroscopy, Astrophys. J. Suppl. Ser. 261 (2) (2022) 35.
- [30] C. Ferrara, M. Giarrusso, F. Leone, Experimental atomic data of spectral lines-I. Cs, Ba, Pr, Nd, Sm, Eu, Gd, Tb, Dy, Ho, Er, Tm, Yb, Lu, Hf, Re, and Os in the 370–1000 nm interval, Mon. Not. R. Astron. Soc. 527 (3) (2024) 4440–4466.
- [31] C. Ryder, Oscillator Strength Measurements in Singly-Ionized, Doubly-Ionized and Neutral Lanthanides and Transition Elements (Sm, Nd, Pr, Gd, Cu, and Fe) using laser-induced breakdown spectroscopy. (Ph.D. thesis), Wayne State University, 2011.
- [32] S. Irvine, H. Andrews, K. Myhre, J. Coble, Radiative transition probabilities of neutral and singly ionized rare earth elements (La, Ce, Pr, Nd, Sm, Gd, Tb, Dy, Ho, Er, Tm, Yb, Lu) estimated by laser-induced breakdown spectroscopy, J. Quant. Spectrosc. Radiat. Transfer 297 (2023) 108486.
- [33] B. Barbieri, N. Beverini, A. Sasso, Optogalvanic spectroscopy, Rev. Modern Phys. 62 (3) (1990) 603.
- [34] P.R. Sen Sarma, M.T. Belmonte, S. Mar, Characterisation of a hollow-cathode lamp to measure accurate branching fractions of rare-earth elements, Eur. Phys. J. D 78 (6) (2024) 76.
- [35] Excelitas Technologies, pco.edge 4.2 bi USB sCMOS camera, 2025, https://www.excelitas.com/product/pcoedge-42-bi-usb-scmos-camera. (Accessed 28 April 2025).
- [36] P.R.S. Sarma, M.T. Belmonte, S. Mar, Analysis of slit curvature using image processing, 2024, http://dx.doi.org/10.5281/zenodo.14002840.
- [37] S. Llorente Rodríguez, et al., Análisis de un plasma de neodimio para medidas espectroscópicas de interés astrofísico, 2024, Universidad de Valladolid. Trabajo Fin de Grado. https://uvadoc.uva.es/handle/10324/70959.
- [38] C.C. Enz, E.A. Vittoz, Charge-Based MOS Transistor Modeling: the EKV Model for Low-Power and RF IC Design, John Wiley & Sons, 2006.
- [39] A. Boukhayma, A. Peizerat, C.C. Enz, Temporal readout noise analysis and reduction techniques for low-light CMOS image sensors, IEEE Trans. Electron Devices 63 (1) (2015) 72–78.
- [40] R.J. Peláez, S. Mar, J.A. Aparicio, M.T. Belmonte, Integration of an intensified charge-coupled device (ICCD) camera for accurate spectroscopic measurements, Appl. Spectrosc. 66 (8) (2012) 970–978.
- [41] H. Xu, S. Svanberg, R. Cowan, P.-H. Lefebvre, P. Quinet, E. Biémont, Theoretical and experimental lifetime and oscillator strength determination in singly ionized neodymium (Nd II), Mon. Not. R. Astron. Soc. 346 (2) (2003) 433–440.
- [42] S. Mar, Atomic transition probabilities with uncertainties, 2024, http://dx.doi. org/10.5281/zenodo.13173712.
- [43] L. Minnhagen, Spectrum and the energy levels of neutral argon, ar i, J. Optical Soc. Amer. 63 (10) (1973) 1185–1198.
- [44] G. Norlén, Wavelengths and energy levels of Ar I and Ar II based on new interferometric measurements in the region 3 400-9 800 å, Phys. Scr. 8 (6) (1973) 249
- [45] P. Quinet, P. Palmeri, E. Biémont, J. Brault, Energy levels in Ar I I, Phys. Rev. A 49 (4) (1994) 2446.
- [46] W. Wiese, J. Brault, K. Danzmann, V. Helbig, M. Kock, Unified set of atomic transition probabilities for neutral argon, Phys. Rev. A 39 (5) (1989) 2461.
- [47] E.D. Tidwell, Transition probabilities of argon II, J. Quant. Spectrosc. Radiat. Transfer 12 (3) (1972) 431–441.